Spectral Water Wave Dissipation by Biomimetic Soft Structure

Garance Marlier, Frédéric Bouchette, Samuel Meulé, Raphaël Certain, Jean-Yves Jouvenel

Journal of *Marine Science and Engineering*

MDPI

Article

Spectral Water Wave Dissipation by Biomimetic Soft Structure

Garance Marlier [1,2,3,*], Frédéric Bouchette [1,2], Samuel Meulé [2,4], Raphaël Certain [2,5] and Jean-Yves Jouvenel [3]

[1] University of Montpellier, CNRS, Montpellier, France; frederic.bouchette@umontpellier.fr
[2] GLADYS, University of Montpellier, Le Grau-du-Roi, France; meule@cerege.fr (S.M.); certain@univ-perp.fr (R.C.)
[3] P2A Développement, 34110 Vic-La-Gardiole, France; jouvenel@p2adev.com
[4] Aix-Marseille University, CNRS, IRD, INRAE, CEREGE, Aix-en-Provence, France
[5] CEFREM, UMR CNRS 5110, Université de Perpignan Via-Domitia, 66000 Perpignan, France
* Correspondence: garance.marlier@hotmail.com

Abstract: Coastal protection solutions can be categorised as grey, hybrid or natural. Grey infrastructure includes artificial structures like dykes. Natural habitats like seagrasses are considered natural protection infrastructure. Hybrid solutions combine both natural and grey infrastructure. Evidence suggests that grey solutions can negatively impact the environment, while natural habitats prevent flooding without such adverse effects and provide many ecosystem services. New types of protective solutions, called biomimetic solutions, are inspired by natural habitats and reproduce their features using artificial materials. Few studies have been conducted on these new approaches. This study aims to quantify wave dissipation observed in situ above a biomimetic solution inspired by kelps, known for their wave-dampening properties. The solution was deployed in a full water column near Palavas-les-Flots in southern France. A one-month in situ experiment showed that the biomimetic solution dissipates around 10% of total wave energy on average, whatever the meteo-marine conditions. Wave energy dissipation is frequency-dependent: short waves are dissipated, while low-frequency energy increases. An anti-dissipative effect occurs for forcing conditions with frequencies close to the eigen mode linked to the biomimetic solution's geometry, suggesting that resonance should be considered in designing future biomimetic protection solutions.

Keywords: wave attenuation; bioinspired structure; biomimetics; soft-shoreline engineering

Citation: Marlier, G.; Bouchette, F.; Meulé, S.; Certain, R.; Jouvenel, J.-Y. Spectral Water Wave Dissipation by Biomimetic Soft Structure. *J. Mar. Sci. Eng.* **2024**, *12*, 2004. https://doi.org/10.3390/jmse12112004

Academic Editor: Decheng Wan

Received: 14 October 2024
Revised: 28 October 2024
Accepted: 31 October 2024
Published: 7 November 2024

1. Introduction

The will to develop coastal defense systems is as old as the desire to secure shorelines for improving human safety and developing maritime trade [1–3]. Until now, traditional artificial protection solutions, such as dykes and groins, have been extensively built throughout the world's shorefaces. However, those so-called grey or hard solutions are currently recognised for their poor longevity in the face of climate change and for their negative impact on the environment, like coastal habitat loss or erosion [4–7].

A first alternative strategy to protect the coast relies on the concept of soft-shoreline engineering (SSE), which emerged in the 1990s in the United States and Canada [3]. SSE solutions encompass protective structures that limit their ecological impact without compromising their technical integrity [2,3]. Some SSE solutions are built with artificial materials (concrete, rock) and form artificial reefs that mimic coral or oysters [8,9], and on which life can develop and improve the coastal defence service. The feedback on these solutions is encouraging, while their long-term behaviour under global change remains speculative [8]. Within the SSE solutions, engineers have also considered the protection of the coast based on natural habitats (seagrass, mangroves and corals) without any recourse on artificial features [6,7,10,11]. These habitats provide a natural barrier against climatic and coastal events, controlling hydrodynamic conditions and sediment motion [7]. Alongside with their protective hydro-morphodynamic services, natural habitats offer various ecological

benefits, including improved water quality and carbon storage [6,10]. As a result, natural habitats are receiving increasing attention for coastal management community [6]. However, their wider adoption in coastal management procedures depends upon more efficient cost–benefit feedback and the development of robust deployment strategies [6,7].

A second alternative strategy for coastal protection is to combine natural habitats and artificial structures in so-called "hybrid" solutions [9]. This approach maximises the protective capacity of any natural habitat while minimising their weaknesses [6]. Hybrid solutions offer an interesting compromise, especially in heavily urbanised coastal areas where the deployment of purely natural solutions may be challenging [6]. In this context, some hybrid solutions are called biomimetic because the hydro-morphodynamic services they offer rely on mechanisms inspired by nature (also called bioinspiration) [9,12]. Developing a biomimetic solution starts with a deep understanding of some natural eco-bio-hydro-morphodynamic processes, which are then stimulated in the real coastal environment through the deployment of artificial features that mimic its effects. For instance, a biomimetic solution made of a dense network of artificial strips, built based on an analogy with seagrass meadow, would alter hydrodynamics [11,13], especially wave damping, and can provide a safe place for the seedlings of seagrass [14]. To our knowledge, no field studies have been carried out on the development and deployment of biomimetic solutions mimicking kelps as a protective solution in coastal engineering [9].

The objective of this study is to provide an initial estimate of the spectral dissipative properties of a representative biomimetic protection solution imitating kelps from in situ measurements in the nearshore zone. First, in Section 2, we describe the state of the art in wave dissipation by natural habitats and the theoretical formulation used to compute the dissipation. Then, the study area, the features of the biomimetic structure, the experimentation and the methodology for data processing are described in Section 3. A comprehensive analysis of the mean and spectral wave dissipation rates is presented in Section 4. Observed dissipation is compared with existing studies. Section 5 reveals and discusses several processes and their consequences for the design of biomimetic solutions. A new empirical drag coefficient law is proposed to improve the structure representation in the numerical model at the end of the discussion.

2. Wave Dissipation by Natural Habitats

2.1. State of the Art

The conception of biomimetic solutions relies on the exploration of the impact of coastal natural habitats on hydro-morphodynamics. Indeed, natural habitats drive changes in fluid velocity profiles [15–17], inferred turbulence [18–20], wave dissipation [21–23] and sediment motion [24–27]. Coral reefs [28,29], salt marshes [30–33], seagrass/kelp beds [13,21,34–39] and mangroves [40,41] dissipate 70%, 72%, 36% and 31% of waves on average, with variations from one study to another ([10], review of 69 projects). Although wave dissipation has been largely investigated in laboratory settings [23,31,32,34,38,41–44] and analytically [21,39,43,45–47], it has been less studied in the field [13,30,36,37]; additionally, few studies have investigated dissipation above giant kelps, and none, to our knowledge, have examined biomimetic solutions inspired by kelps. It is difficult to dissociate wave dissipation driven by bottom friction from a kelp effect [48]. Elwany et al. [49] suggest that kelps have practically no effect on wave dissipation with periods of 5–20 s, but they used bottom-mounted pressure sensors, which limit the detection of shorter waves. Rosman et al. [50] quantified wave energy both inside and outside of a giant kelp forest and did not find clear evidence of wave dissipation through the forest for a similar wave forcing. Elsmore et al. [51] found that giant kelps dissipate around 7% of the wave energy flux, contrary to a transect without kelps. Lindhart et al. [48] indicated that short waves are more dissipated when the kelp surface canopy is high, i.e., in summer. However, wave dissipation and its frequency-dependence have received very little attention in the literature [48], despite observations which tend to show that kelps have a non-negligible dissipation effect [51].

2.2. Theoretical Formulation of Wave Dissipation

Historically, the theoretical formalization of wave dissipation on soft structures is based on Dalrymple et al. [52], in which dissipation is defined based on a wave energy balance equation. Dalrymple et al. [52] hypothesise that vegetation can be represented by rigid vertical cylinders. Assuming that waves propagate along an x-axis, the conservation of wave energy is defined as

$$\frac{\partial E c_g}{\partial x} = -\epsilon_s. \tag{1}$$

Here, $E = \frac{1}{8}\rho g H_s^2$ is the wave energy density of wave given by the linear theory, ρ is the density of water, g is the gravitational acceleration, H_s is the significant wave height, c_g is the wave group velocity and ϵ_s is the time-averaged rate of energy dissipation per unit horizontal area driven by the structures opposing the waves:

$$\epsilon_s = \frac{1}{T}\int_0^T \int_{z=0}^{l_s} (F_x u + F_z w) dz dt \tag{2}$$

where l_s is the structure length, F_x and F_z are the horizontal and vertical components of the total force acting on the structure at a given z, and u and w are the horizontal and vertical components of the fluid velocity. The horizontal component F_x is considered to be much greater than F_z [34,45]. As the structure is considered rigid, no movement occurs along the z-axis. According to Morison's equations [53], the force F_x applied to a rigid structure is

$$F_x = \frac{1}{2}\rho S_{ref} C_D |u| u + \frac{\pi}{4} N b_v^2 \rho C_M \frac{\partial u}{\partial t} \tag{3}$$

in which S_{ref} is a surface reference, b_v the structure area per unit height, N the density, C_D is the drag coefficient and C_M is the inertia coefficient. The reference surface S_{ref} is the surface perpendicular to the flow per unit volume on which the energy loss is calculated. Its definition varies depending on whether the study is concerned with the spacing between structures s [52], their density N [21] or other geometric characteristics [32,38]. In this study, the form $S_{ref} = N b_v$ defined by Mendez and Losada [21] is used. The first term of Equation (3) represents the drag force F_D and the second the inertia force F_M. The contribution of the inertia force to wave dissipation is smaller than the drag force and is usually assumed to be zero [21,34,54]. Assuming that the depth is constant along the propagation axis, c_g is constant. By combining Equations (1) and (2), the solution to the differential equation is

$$\frac{H_s}{H_{s_0}} = \frac{1}{1 + K_D H_{s_0} x}. \tag{4}$$

H_{s_0} is the significant wave height at the entrance of the transect in deep water. In Dalrymple et al. [52], K_D is the dissipation coefficient, defined by

$$K_D = \frac{4}{9\pi} C_D k S_{ref} \frac{\sinh^3 k l_s + 3 \sinh k l_s}{\sinh kh (\sinh 2kh + 2kh)} \tag{5}$$

where S_{ref} is the variable defined above, k is the wave number and h is the depth. To correctly apply this analytical model, the drag coefficient can be estimated using various strategies [21,23,32,36,38,55].

Kobayashi et al. [34] demonstrate that C_D depends on the Reynolds number $R_e = \frac{u_c D}{\nu}$, where D is the diameter of one structure, u_c is the characteristic velocity and ν is the kinematic viscosity of water, and express this empirical drag coefficient in the form of a law:

$$C_D = \alpha + \left(\frac{\beta}{R_e}\right)^{\gamma} \tag{6}$$

where α, β and γ are coefficients determined experimentally. The characteristic velocity u_c is defined as the maximum amplitude of the orbital wave motion at the top and on the front side of the structure [22,45,56] and is written as

$$u_c = \frac{\pi H_{s_0}}{T_m} \frac{\cosh kl_s}{\sinh kh} \tag{7}$$

where T_m is the mean wave period. The law in Equation (6) has been widely used [22,36,45,57] and reformulated with the Keulegan–Carpenter number $K_C = \frac{u_c T_m}{D}$ [21–23,39]. The preeminence of K_C or R_e in the formulation of C_D is still under debate [58].

In Dalrymple et al. [52], formalism is applied to study wave dissipation either over natural or artificial structures, although they are flexible [21,22,34,56]. Alternative works have tried to include flexibility in the original formalism [32,36,38,45,46,59]. Méndez et al. [45] consider the swaying of the structure thanks to relative horizontal velocity u_r, defined as the difference between the velocity of the structure and that of the fluid. This parameter is introduced directly in Equation (3) instead of the horizontal velocity u. Luhar and Nepf [60] employ an effective length l_e which represents the length of a rigid structure that generates the same drag force as a flexible structure of length l_s. Lei and Nepf [38] apply this length correction directly in Equation (5) from Dalrymple et al. [52] to predict the wave attenuation over a flexible seagrass meadow. In parallel, Dalrymple et al. [52], formalism is improved to take into account irregular waves, using H_{RMS} (root-mean-squared wave description) instead of H_s in the definition of the dissipation [21]. Suzuki et al. [61] adopted this new equation for implementing canopy dissipation in the spectral model SWAN (Simulating Waves Nearshore), adding dependencies to the frequency and wave directions. Jacobsen et al. [62] adopt Suzuki's method to take into account the effect of frequency on the velocity profile inside and outside the canopy, and Ascencio et al. [63] apply Jacobsen's work in a laboratory. However, we do not consider these fully spectral/directional developments because (i) this experimentation provides no information about wave direction and (ii) this work is limited to a spectral analysis averaged over frequency bands of physical meaning.

3. Material and Methods

3.1. Study Area

This study was carried out near the outlet of the Lez river and the entrance to the port of Palavas-les-Flots in the south of France (Figure 1a,b). The coastline is densely urbanised, with numerous dykes, and attracts a significant number of tourists during the summer season, which makes this place strategic for coastal management. A dyke, oriented north–south, is located to the west to delimit the port area. The study area is a microtidal environment of almost constant water depth (3–3.5 m) in the studied area. The sediment is sandy, with some mud in the Lez channel. The beaches of Palavas-les-Flots are subject to different wind regimes throughout the year. Winds come mainly from the north, west and south-east during storms. The orientation of the bay is directly affected by south-east storms. However, the orientation of the breakwater, located at the left side of the study site, protects the entrance to the port and the channel from waves from the south or the west. The proximity of the study site to grey structures was constrained by administrative authorisations. The possible impact of the dykes on the measurements is discussed in Section 5.1.

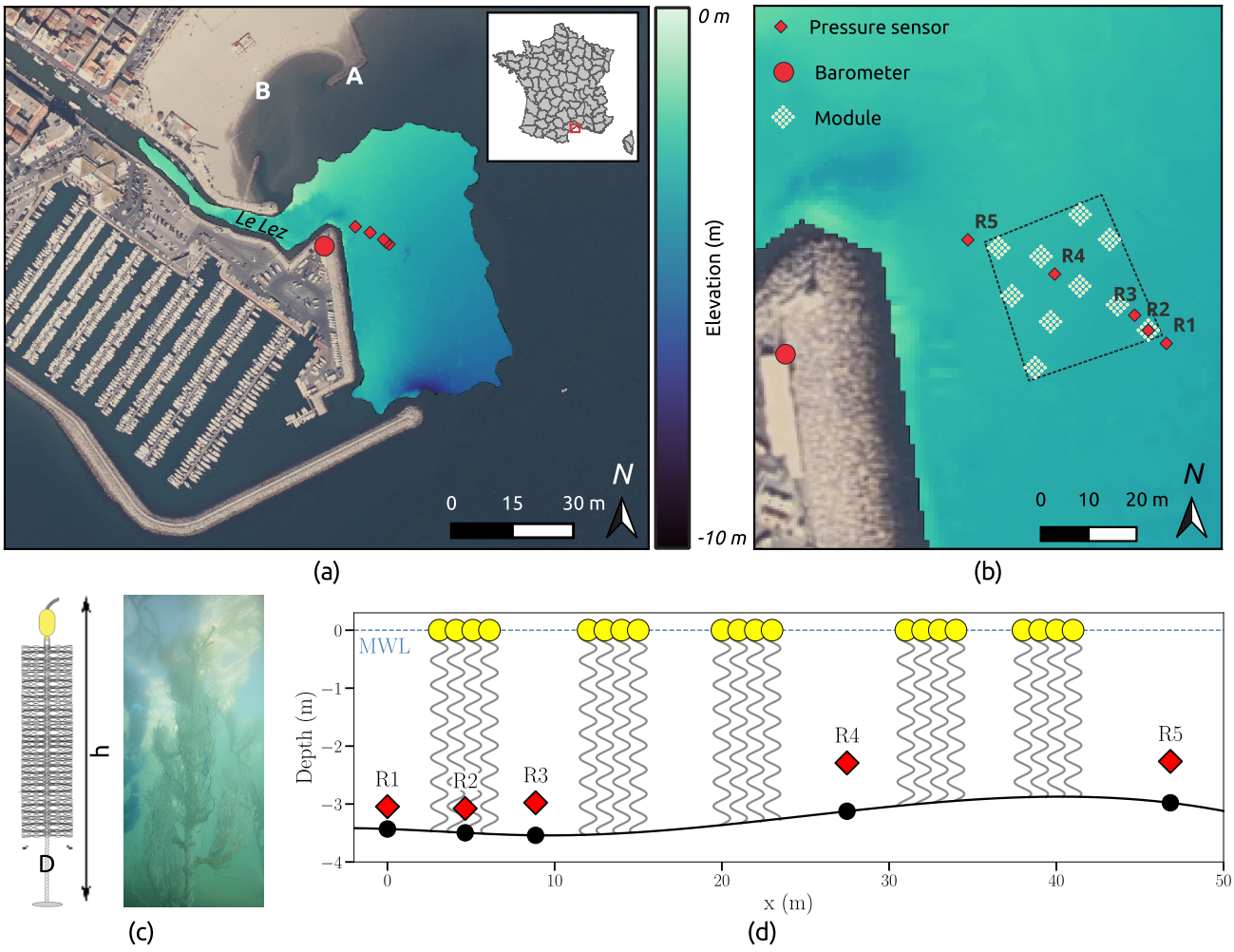

Figure 1. (**a**) A map of the study area, where A and B refer to the dyke and the beach in Section 5.1. (**b**) A map of the position of the device and the biomimetic structures, composed of ten modules. The black dotted lines forming a rectangle delineate the extension of the biomimetic solution and the domain on which Rabinovitch formalism was used (Section 5.1). The coloured area represents the bathymetry. (**c**) The diagram and the photo show one biomimetic structure. (**d**) A plot of the instrumented transect, where pressure sensors (red diamond) and idealised biomimetic structures are shown. The seabed (black solid line) is placed as a function of the depth measurements (black dots) made at each device.

3.2. The Biomimetic Structure

The biomimetic structures considered in this study were inspired by aquatic vegetation, in particular, kelps, especially *Macrocystis pyrifera* and developped by P2A Développement. Macrosystis are located mostly over rocky substrate at a depth between 5 and 25 m and occupy the water column when they are mature, and extend toward the surface [48]. The fronds are buoyed by pneumatocysts and are 10 to 40 cm long [51]. The biomimetic structure is designed to attenuate wave height while providing shaded zones and places sheltered from view that favour the presence of many aquatic species. The structure is made of polypropylene ropes, with a Young's modulus of 9.8 MPa. One end of the central rope is secured to a jetting anchor buried in the sand, while the other end is attached to a buoy to keep it upright, similarly to *Macrocystis pyrifera*. The structure has a total length l_s of 3.5 m and emerges at the water surface. Fronds are uniformly spaced along the main rope at 10 cm intervals and are 40 cm long with a diameter of 1.6 cm. The representative diameter D of a structure is set to 3 cm, which corresponds to the diameter of the central

rope without the fronds. The diameter value is discussed in Section 5.2. Sixteen structures are assembled in modules of 16 m^2, in which they are spaced at regular 1 m intervals with respect to their center. Thus the density N of structure per unit area in a module is 1. In the following section, the set of modules deployed together is described, called the biomimetic solution.

3.3. Field Data Collection

A linear transect of 5 pressure sensors, R1–R5 (RBR virtuoso 3, RBR, Ottawa, ON, Canada), was deployed across the biomimetic solution between March and April 2023 (Figure 1c). Pressure time series were collected continuously at a sampling rate of 8 Hz. The initial accuracy of the pressure sensors was ±1.0 cm with a resolution of 2 mm. Each pressure sensor was positioned on a metal structure at an elevation Z_m above the seabed. The characteristics of the pressure sensors are given in Table 1. The instrumented transect was oriented at 120°/300°, very similar to the wave direction during storms. The transect was 47 m long with a flat bottom. An atmospheric pressure sensor, B1 (Solinst Barologger, Solinst, Georgetown, ON, Canada), was positioned next to the deployment zone and continuously collected one measurement per minute.

Table 1. Characteristics of pressure sensor deployment.

Station	R1	R2	R3	R4	R5
Distance (m)	0	4.65	8.86	27.48	46.82
Depth (m)	2.45	3.07	2.97	2.29	2.26
Z_m (m)	0.99	0.42	0.56	0.83	0.71

The average wind speed and direction were obtained from the weather station at Montpellier airport, managed by Météo-France and located 7 km north of Palavas-les-Flots. These data are averaged over 10 min every hour. Offshore wave forcing is extracted from the Sète wave buoy from the French national coastal wave CANDHIS network managed by Cerema and DREAL Occitanie, in the form of the significant wave height, mean period and direction every 30 min.

3.4. Field Data Analysis

The measured pressure data (from R1–R5) were corrected from atmospheric pressure using the measurements of B1. The signal was split into 30 min bursts with a 50% overlap. The wave spectra were calculated over each burst by Fast Fourier Transform. The energy spectral density obtained was depth-corrected with the linear theory [64], revealing a cut-off frequency of 0.55 Hz. For each spectrum, wave parameters such as the significant wave height H_s and the mean wave period T_m were extracted. H_s and T_m are defined by

$$H_s = 4\sqrt{\int_{f_1}^{f_2} E(f)df} \qquad T_m = \sqrt{\frac{\int_{f_1}^{f_2} E(f)df}{\int_{f_1}^{f_2} E(f)f^2df}} \tag{8}$$

where $E(f)$ is the energy spectral density, f_1 and f_2 are the limits of a frequency band over which the wave parameters are calculated and f the frequency.

To analyse the sensitivity of wave dissipation to wave frequency, the spectra were divided into 3 frequency bands. The frequency cuts between these bands were defined from the mean of the 2853 elementary spectra (Figure 2). The first band, between 0.004 and 0.04 Hz, is identified as the infragravity (IG) band [65]. The second band, between 0.04 and 0.114 Hz, corresponds to swell (SS), and the last band, between 0.114 and 0.55 Hz, corresponds to wind waves (WW) [66]. The upper limit of the wind wave band was set at the cut-off frequency, beyond which the signal corrected by linear theory diverges with respect to the hydrostatic signal. H_s and T_m were calculated at each burst for each of these bands.

In the following, H_s and T_m are named $H_{i,j}$ and $T_{i,j}$ where i refers to the station and j to the frequency band. For example, at the R1 station, the significant wave height and the mean period for the IG band are $H_{1,IG}$ and $T_{1,IG}$, respectively. The wave height and period derived after the total spectrum are referred as TOT.

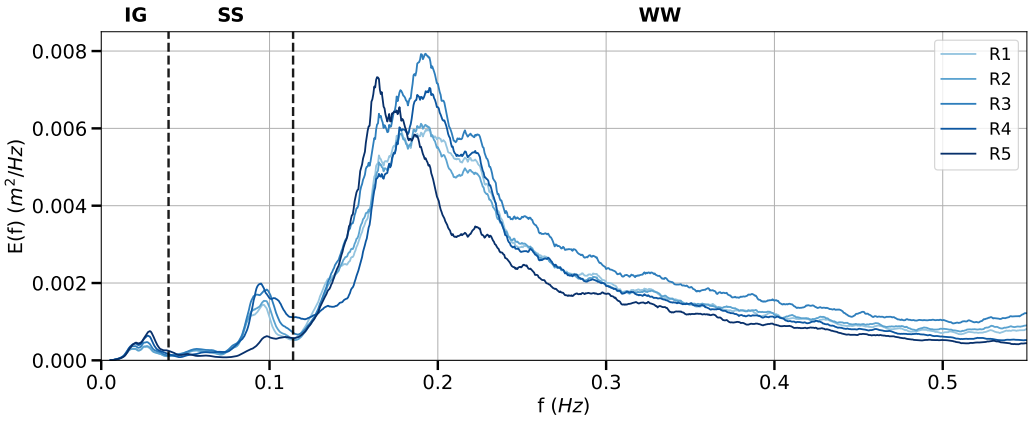

Figure 2. Energy spectral density spectra calculated at stations R1 to R5. Each spectrum is calculated by averaging all the spectra calculated over the 30 min long bursts. The dotted vertical lines represent the frequency cuts of the infragravity, the swell and the wind wave bands, clearly identified by relative minima on every mean spectrum.

4. Results

4.1. Forcing Conditions Offshore and at R1 Station

The recorded tidal range does not exceed 0.3 m during the experimentation. The breaking index $\gamma = H/h$ defined by Munk [67], with a threshold of 0.78, and the more restrictive index by Nelson [68] for irregular waves, with a threshold of 0.55, are calculated for each burst at all measurement stations. The maximum of $\gamma = H/h$ obtained during the experimentation is 0.19 at the R5 station, so no wave breaking is identified in the studied domain. The relative shallowness kh calculated based on the linear theory ranges from 0.47 to 3.00, which means that the experimentation occurred entirely in intermediate-water-depth conditions, far from the dominant breaking zone. The wave nonlinearity is calculated at each burst and each station from the Ursell number, defined as $U_r = H_{i,TOT}\lambda_i^2/h_i^3$, where λ_i is the wavelength calculated with the approximation of Guo [69], and ranges from 0.07 to 10.49 (maximum obtained at R5 station). According to Hedges [70], the wave nonlinearity threshold is set at $U_r = 40$, which is larger than the maximum values calculated. The wave steepness, defined as $H_{i,TOT}/\lambda_i$, does not exceed 0.034 (maximum value obtained at R3 station), which is below the value defining the Stokes second-order domain [70]. So, wave nonlinearity is not considered in this study.

Different wind and wave conditions are observed, from which three types of meteo-marine conditions are identified (Figure 3). Type 1 corresponds to a windy regime, known as "Tramontane" in the south-west of France, that occurred twice between 31 March and 2 April 2023 (T1a) and between 12 and 16 April 2023 (T1b). The forcing parameters during type 1 conditions are as follows: $u_{wind,T1} = 7.9$ m/s on average with a westerly to west–northwesterly direction. The ranges of the other parameters are $H_{offshore,T1} = 0.24$–1.18 m, $T_{offshore,T1} = 2.7$–3.78 s, $H_{1,T1} = 0.02$–0.12 m and $T_{1,T1} = 3.16$–7.0 s, where $u_{wind,Ti}$, $H_{offshore,Ti}$ and $T_{offshore,Ti}$ refer to measurements made offshore and at the airport of Montpellier (see Section 3.3). Type 2 is a thermal northerly/southerly wind regime alternating day and night, where $H_{offshore,T2} = 0.13$–0.71 m, $T_{offshore,T2} = 2.52$–5.26 s, $H_{1,T2} = 0.03$–0.2 m and $T_{1,T2} = 2.25$–7.96 s. Two type 2 events are recorded between 2 and 7 April 2023 (T2a) and between 16 and 20 April 2023 (T2b). Type 3 conditions are representative of a moderate storm and occurred twice during the experimentation, between 29 and 31 March 2023 (T3a) and between 20 and 23 April 2023 (T3b), the first being less energetic than the second. The parameters associated with type 3 conditions are $u_{wind,T3} = 4.94$ m/s on average

from the south-east direction, $H_{offshore,T3} = 0.27$–1.45 m and $T_{offshore,T3} = 2.64$–4.31 s, $H_{1,T3} = 0.05$–0.56 m and $T_{1,T3} = 2.36$–4.31 s.

In the following section, an analysis of wave dissipation is conducted for the three types of conditions emblematic of the regional meteo-marine regimes. The values of the R_e and K_C numbers observed under these three types of condition are reported in Section 5.2.

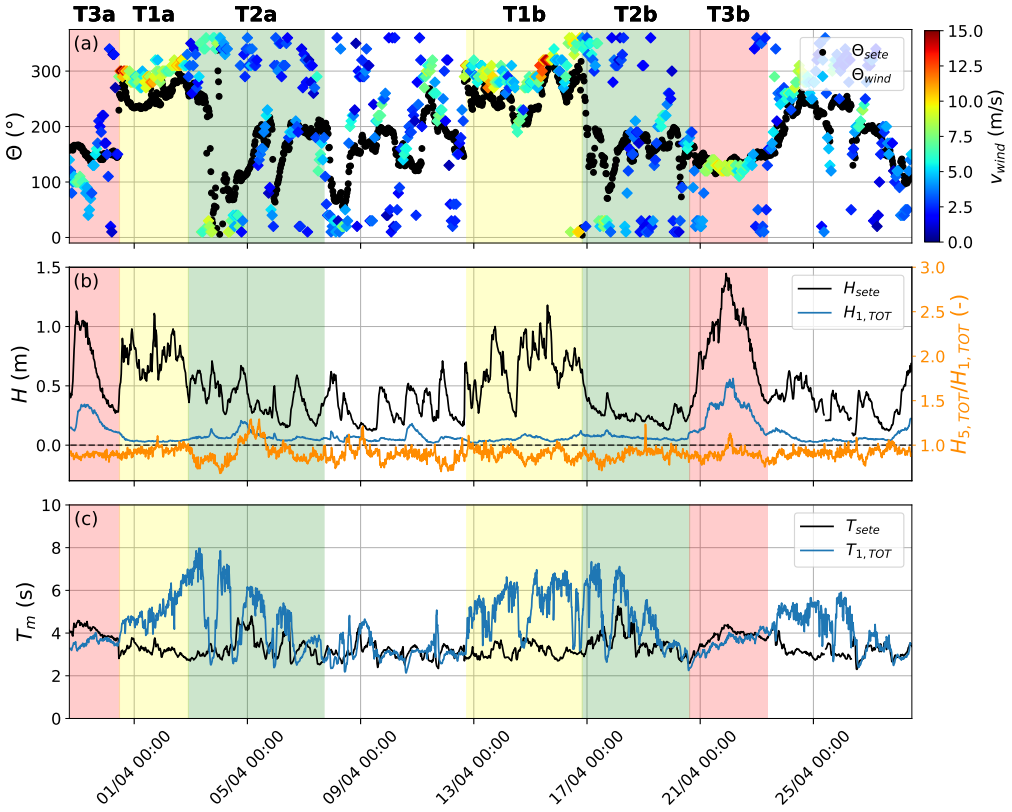

Figure 3. Wind and hydrodynamic forcings during the experimentation. The yellow, green and red boxes represent type 1, 2 and 3 conditions, respectively, observed in two periods, a and b. Periods in white are not used in the analysis. The wave characteristics at Sète are offshore conditions. (**a**) Wave direction (θ_{sete}) at Sète, wind direction (θ_{wind}) and wind speed (v_{wind}) recorded at the Montpellier airport weather station; (**b**) Significant wave height measured at Sète (H_{sete}) and at R1 station, and the ratio $H_{5,TOT}/H_{1,TOT}$; (**c**) The mean wave period measured at Sète ($T_{m_{sete}}$) and at the R1 station.

4.2. The Conditions over the First Module of the Biomimetic Solution

The significant wave height averaged over all the bursts increases by 0.9 ± 1.0 cm between the R1 and R3 stations (i.e., through the first module), and by 3.0 ± 1.0 cm during type 3 conditions. In the literature, the increase in significant wave height at the front side of a dissipative structure has already been predicted analytically [45] and justified by partial wave reflection against the structure. Such an increase in wave height has also been observed in the field [36]. Alternatively, the biomimetic structure could be blocking the full water column, behaving as a low-crested hard structure. In such a case, when waves land on the first module, the wave speed would slow down and the wave height would increase. To estimate such a shoaling contribution between the R1 and R3 stations, a simple shoaling equation can be used [71]. This calculation determines that the mean difference in wave height driven by shoaling between the R1 and R3 stations is 0.8 cm. In type 3 conditions, this difference is 3.0 cm. These values corroborate those observed in the experimentation. Beyond the first module, from the R3 to R5 stations, clear wave decay occurs.

4.3. Mean Wave Dissipation by the Biomimetic Solution

Figure 4a shows the evolution of the energy in each frequency band through the biomimetic solution and for the three types of meteo-marine conditions.

The dissipation of the total wave energy averaged over all bursts is around 10%, with a standard deviation of 7.7%, whatever the meteo-marine conditions (Figure 4a; $H_{5,TOT}/H_{1,TOT}$ around 0.9), and it decreases linearly after the first module (R3 station). Moreover, considering the increase in wave energy between the R1 and R3 stations by 5–10% (see previous section), the total wave dissipation after this local shoaling effect is around 15–20%, whatever the meteo-marine conditions.

But there is no direct evidence on whether this wave decay is the result of dissipation by bottom friction, breaking waves, energy transfer to currents or the biomimetic solution itself. Bottom friction is assumed to be negligible, considering that the mean friction factor for this site is around 1.2×10^{-4} based on the formulation of Phillips [72]. Dissipation by geometric breaking is non-existent, as discussed in Section 4.1. Thus, the decrease in waves must be attributed mainly to a dissipation process induced by the biomimetic solution.

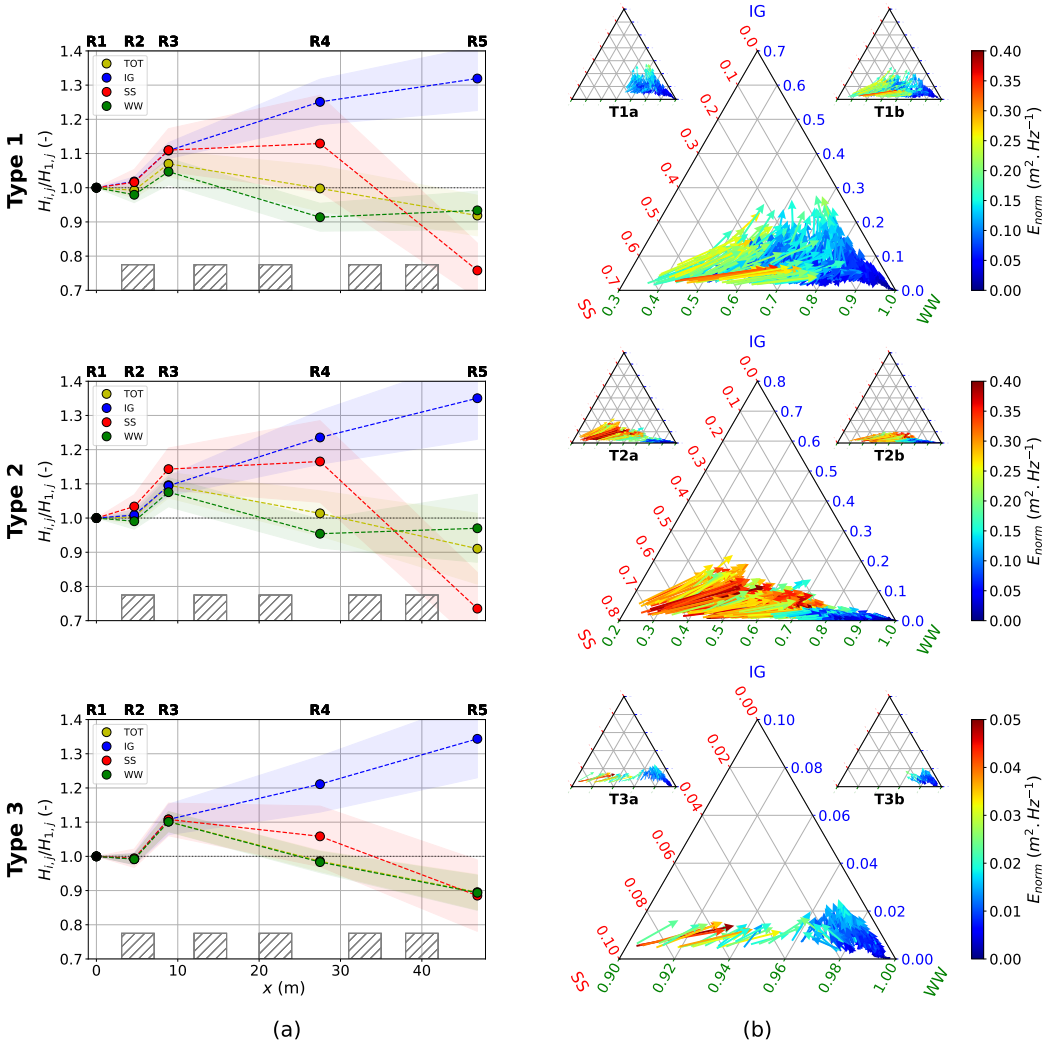

Figure 4. (**a**) Plots of mean wave height reduction for *TOT*, *IG*, *SS* and *WW* frequency bands from the R1 to R5 stations for the three types of meteo-marine conditions, including both periods a and b. The coloured envelope represents the standard deviation at each station and for each frequency band. (**b**) Ternary diagrams of normalised E_{IG}, E_{SS} and E_{WW} by E_{TOT} for the three types of meteo-marine conditions. The two smaller ternary diagrams represent the same information for periods a and b considered separately. Each arrow represents the evolution of the relative contributions of *IG*, *SS* and *WW* to the energy between the R1 and R5 stations for each burst.

At the R5 station, the energy in the IG band increases by more than 30% with respect to the R1 station and 20% with respect to the R3 station (Figure 4a). The SS band energy is mainly dissipated over the second part of the biomimetic solution (after the R4 station) and not after the first module (R3 station), although a slight decrease is observed there for type 3 conditions (Figure 4a). In bulk, at the R5 station, up to 25% (35–40% with respect to the R3 station) of the SS band energy is dissipated for type 1 and 2 conditions with respect to the R1 station, compared with 10% with respect to the R1 station (20% with respect to the R3 station) for type 3 conditions. The energy contained in the WW band globally decreases across the biomimetic solution, although a small increase is observed between the R4 and R5 stations for type 1 and 2 conditions. The WW band energy loss represents a total dissipation of 7%, 5% and 10% with respect to the R1 station (10%, 10% and 20% with respect to the R3 station) for types 1, 2 and 3, respectively (Figure 4a).

To decipher whether the relative evolution of the wave energy of the the frequency bands at the R3, R4 and R5 stations is driven by energy transfer between frequency bands and/or dissipation, the absolute wave energy values of the frequency bands are compared at those stations. Table 2 represents the average values of the absolute energy in each frequency band calculated per meteo-marine condition. In all cases, the spatial variation (from the R1 to R5 stations) in absolute energy for each frequency band shows the same trend as that of the normalised energy (Figure 4a). Nevertheless, the ratios of absolute energy between frequency bands are high, with values around 10 between the IG and SS bands and 100 between the IG and WW bands for type 1 and 2 conditions. For type 3 conditions, the IG and SS bands' absolute energies are similar, while that of the WW band is 100 times that of the IG and SS bands. In any case, these ratios are far too large to justify the wave decay in the SS and WW bands through single energy transfers to the IG band. So, wave decay most likely results from wave dissipation over the biomimetic solution.

Table 2. Table of mean values of energy density $E_{i,j}$ (mm^2 Hz^{-1}) at each frequency band for R1 to R5 stations for type 1, type 2 and type 3 conditions.

	$E_{i,j}$	R1	R2	R3	R4	R5
Type 1	$E_{i,IG}$	5.77	5.99	7.10	9.05	10.03
	$E_{i,SS}$	42.72	46.05	56.38	63.62	22.39
	$E_{i,WW}$	110.93	106.70	123.54	94.50	94.19
Type 2	$E_{i,IG}$	4.81	4.94	5.87	7.40	8.41
	$E_{i,SS}$	82.28	88.62	108.45	111.42	36.41
	$E_{i,WW}$	283.36	285.97	344.05	252.35	295.85
Type 3	$E_{i,IG}$	26.09	25.78	33.49	40.02	46.80
	$E_{i,SS}$	38.68	38.42	49.68	46.70	31.95
	$E_{i,WW}$	4861.36	4832.46	6044.96	4802.65	4153.89

4.4. Variability in Wave Dissipation Driven by Meteo-Marine Conditions

Figure 4a shows the evolution of the mean dissipation at each frequency band and each station calculated over the 624, 822 and 429 bursts contained in type 1, 2 and 3 conditions (Section 4.1). The figure also shows the standard deviation at each frequency band and each station. The standard deviation represents the variability of the dissipation as a function of the meteo-marine conditions. Taking into account this variability does not change the interpretation of the results presented in Section 4.3. Complementarily, a detailed analysis of wave dissipation at the scale of the burst provides information on the influence of meteo-marine conditions on the behaviour of the biomimetic solution. Figure 4b shows the relative distribution of the energy at each burst in the different frequency bands between the R1 and R5 stations (see Figure 1).

Figure 4b shows that the incoming forcing has significantly lower energy in the IG band than the other frequency bands whatever the meteo-marine conditions. For type 1 and 2 conditions, the energy in the SS and WW bands is greater and more spread out,

although the energy is greater in the WW band on average. For each burst under type 3 conditions, the energy is condensed in the WW band (more than 90%). Longer incoming waves at the R1 station drive higher transfer of energy to the IG band for type 1 conditions (Figure 4b). Intermediate and shorter incoming waves transfer more energy to the IG band for type 2 conditions. In type 3 conditions the relative energy is mostly contained in the WW band (more than 90%); and whatever the incoming forcing, the amount of energy transmitted to the IG band is almost identical between the R1 and R5 stations. The impact of the biomimetic solution on wave dissipation is clearly a function of the SS and WW signatures of the incoming wave conditions.

4.5. Spectral Wave Dissipation

Figure 5 shows the average wave spectra for each type of meteo-marine condition and at each station. For types 1 and 2, the mean wave spectra present 2 peaks around 0.1 Hz (SS band) and between 0.13 and 0.14 Hz (WW band) and a small amount of energy around 0.025 Hz in the IG band. The energy is higher in the WW band than in the SS band for type 2 conditions, contrary to type 1 conditions. For type 3 conditions, a well-marked single energy peak is located in the WW band between 0.16 and 0.25 Hz for all stations.

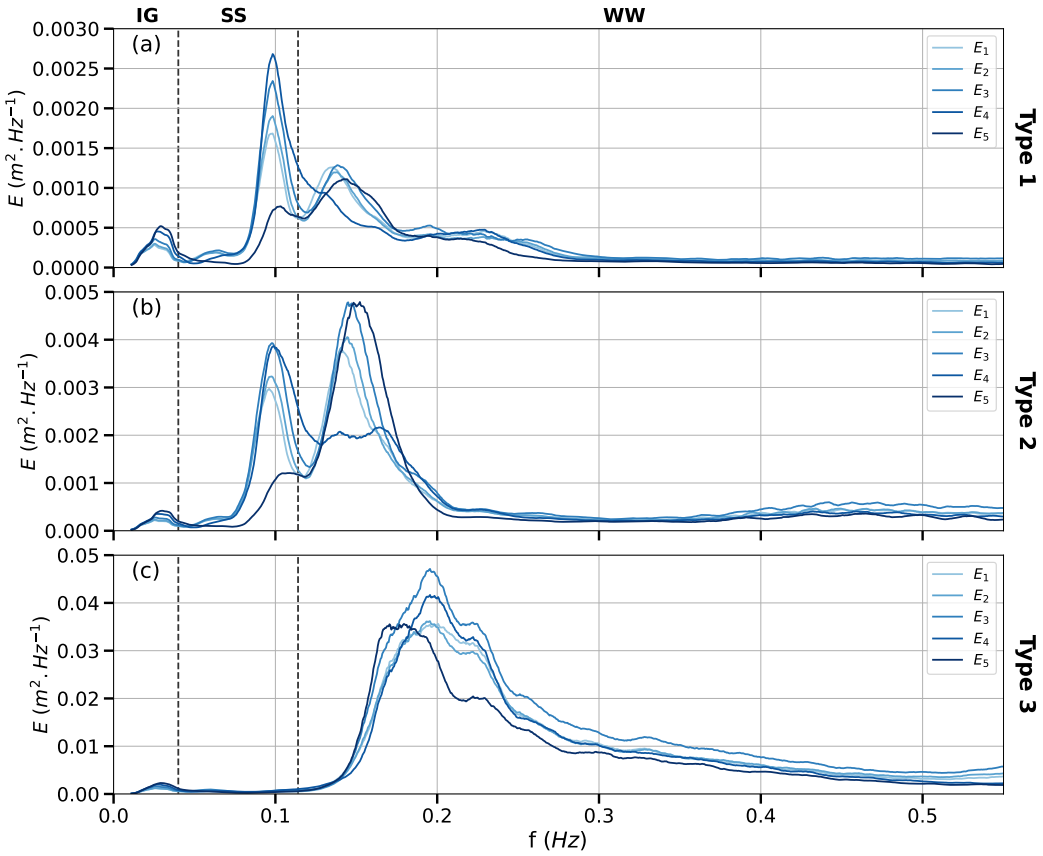

Figure 5. Plots of energy density spectra at R1 to R5 stations for (**a**) type 1, (**b**) type 2 and (**c**) type 3 meteo-marine conditions. Each spectrum is calculated by averaging all elementary spectra calculated over 30 min long bursts for each type of meteo-marine condition.

Whatever the meteo-marine conditions, the energy in the IG band increases between the R1 and R5 stations. The energy contained in the SS band increases between the R1 and R4 stations for type 1 and 2 conditions, then decreases sharply at the R5 station, while the amount of energy in the SS band is negligible for type 3 conditions. For type 1 and 2 conditions, the energy in the WW band increases between the R1 and R3 stations, with a slight frequency shift of around 0.05 Hz towards the high frequencies. At the R4 station, the energy decreases significantly and then increases again until the R5 station. For type 3

conditions, the energy increases until the R3 station, then decreases until the R5 station, with a frequency shift of 0.02 Hz towards the low frequency.

5. Discussion

5.1. Control of Stationary Wave Inferred by Biomimetic Solution on Wave Dissipation

Figure 6 shows the relationship between the dominant wavelength (calculated after the peak period) of the wave forcing with respect to wave dissipation through the full solution ($H_{5,TOT}/H_{1,TOT}$). An anti-dissipative effect occurs for forcing wavelengths around 37 m, corresponding to a peak period of 6.47 s. It appears that this length corresponds to that of the biomimetic solution projected on a segment between the R1 and R5 stations. Moreover, anti-dissipation occurs mainly for intermediate conditions, which are of type 2, possibly type 1 and very rarely type 3 (see also Figure 3, where $H_{5,TOT}/H_{1,TOT} > 1$).

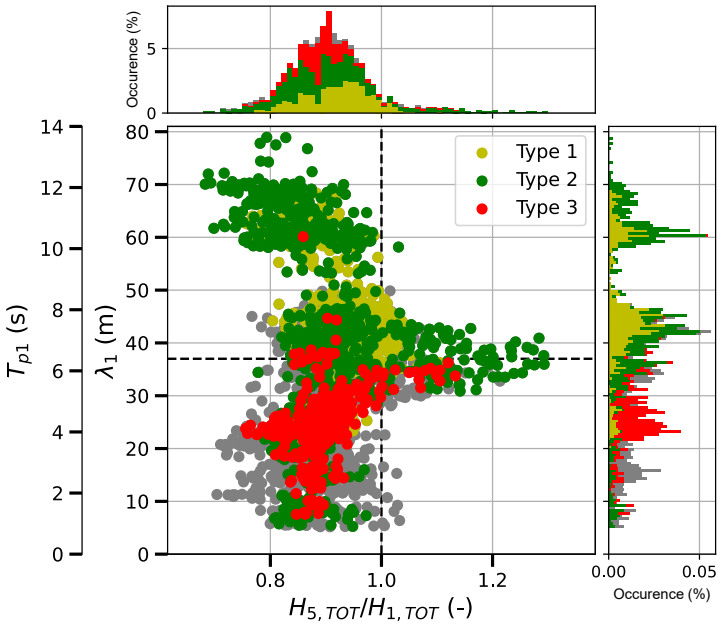

Figure 6. A plot of the wavelength λ_1 and peak period T_{p1} defined at the R1 station as a function of $H_{5,TOT}/H_{1,TOT}$ for each burst. Bursts related to different meteo-marine condition types are represented by different colours. The grey dots represent the burst not related to the different meteo-marine condition types. The wavelength is calculated from each frequency peak for each burst with the approximation of Guo [69]. The peak period is calculated from the peak frequency. The vertical dashed line separates the dissipative ($H_{5,TOT}/H_{1,TOT} < 1$) and anti-dissipative ($H_{5,TOT}/H_{1,TOT} > 1$) domains. The horizontal dashed line is placed at λ_1 = 37 m (T_{p1} = 6.47 s), which is roughly equal to the diagonal length of the biomimetic solution.

Having noticed that a wave characteristic (the peak wavelength) is related to a geometrical property (the length of the biomimetic solution), we propose verifying whether the anti-dissipative effect could be linked to a resonance phenomenon. In a closed basin, Rabinovich [73] defines seiche (also called "harbor oscillation" in semi-enclosed basin) as a long stationary wave whose period varies between a few seconds to hours. In such a context, waves coming from the open sea enter into resonance locally or entirely with the basin geometry. The eigen modes of a closed-basin oscillation can be calculated from its geometrical features and depth. In the case of a semi-open rectangular basin with constant depth, the period of the eigen modes is:

$$T^n = \frac{4L}{(2n+1)\sqrt{gh}} \tag{9}$$

where T^n is the period of the n-th eigen mode and L the length of the basin. The higher the eigen mode (very large n), the less energetic the resonant wave harmonic. Figure 1 shows the external contour of the biomimetic solution as a rectangular zone whose western edge is parallel to the harbour jetty. This domain has a length of 28 m, a width of 25 m and an average depth of 3.3 m. Applying Equation (9), the eigen mode of order 1 has a period of 6.56 s.

Rabinovich [73] also proposes a 2D version of Equation (9) for rectangular basins of length L, width l and constant depth h:

$$T^{mn} = \frac{2}{\sqrt{gh}} \left[\left(\frac{m}{L}\right)^2 + \left(\frac{n}{l}\right)^2 \right]^{-\frac{1}{2}} \quad (10)$$

where T^{mn} is the period associated with the m,n-th eigen mode. By applying Equation (10) on the external contour defined above, an eigen mode is found for $m = 1$ and $n = 1$ that is associated with a period of 6.55 s.

The similarity between Rabinovitch T^1 and T^{11} periods and those observed in the field (Figure 6) suggests that the biomimetic solution may behave like a rectangular semi-enclosed basin open to the south. Such a behaviour would mean that the modules developing throughout the water column act as walls.

However, other features could be at the origin of resonance. First, a resonant basin of 20 m in length could develop between the jetty and the western edge of the biomimetic solution (acting as a wall). For this basin, no eigen mode with a period of the order of 6.5 s is found with the Rabinovitch approach. A second resonant basin could extend between the biomimetic solution and the dyke named A in Figure 1 with a length of 176 m. In this case, the ninth eigen mode with a period of 6.51 s fits the measured period. However, the energy associated with the ninth eigen mode must be negligible in front of the first mode, which, in this case, shows no energy. Thus, the second resonant basin is not an option. A similar result is obtained with a third basin of length 211 m extending between the biomimetic solution and the beach to the north (point B in Figure 1) for which the eleventh eigen mode has an associated period of 6.44 s.

Rabinovitch formalism shows that the biomimetic solution generates resonant waves for forcings with a wavelength of the same order of magnitude as the length of the solution, independently of the geometry of the jetties surrounding the solution. Resonant waves are known as particularly destructive in harbour contexts. The design of the biomimetic solution should consider the generation of long waves within the structure itself. A study of the hydrodynamic context in which the structure will be deployed should be carried out to identify the wavelengths associated with the dominant forcings. The dimensions of the structure could then be adapted to avoid the generation of such waves.

5.2. Defining an Empirical Drag Coefficient for the Biomimetic Solution

Generally, an empirical C_D is calculated after measurements carried out in a laboratory or in the field. In this section, C_D is derived from wave properties and wave dissipation measured during the Palavas-les-Flots experimentation. C_D is then expressed as function of Keulegan–Carpenter K_C and Reynolds R_e numbers and is compared with other analytical expression of C_D from the literature. Although the literature offers several dozens of reference on the question, only articles performing an analysis on flexible or rigid structures extending over the full water column are considered.

First, Equation (5) is rewritten to express C_D as a function of wave number k, some geometrical properties (l_s, h and S_{ref}) and dissipation coefficient K_D which is directly calculated with $H_{i,TOT}$ at the R1 and R5 stations following Equation (4). The Reynolds R_e and Keulegan–Carpenter K_C numbers are derived after measuring the orbital velocity (Equation (7)) and wave period. Then, C_D is plotted as a function of R_e (resp. K_C), and two laws in the form of Equation (6) are fitted on the experimental data (Figure 7a,b). The negative values of C_D are removed, as they correspond to points with no dissipation (see

Section 5.1), i.e., $H_{5,TOT}/H_{1,TOT} > 1$ (total of 239 bursts). The calculated C_D values range from 0.096 to 188.9, decrease with increasing K_C or R_e and develop in a range similar to that described in the literature (see Table 3), although the fitted C_D laws in the case of the biomimetic solution are generally shifted in R_e with respect to that already established (Figure 7c). The spreading of the values is due to the several meteo-marine conditions measured during the experiment, as observed by Paul and Amos [37]. The quality of the fit with Equation (6) is relevant when considering all data and for type 3 conditions, but not for type 1 and 2. The correlation coefficient obtained for energetic conditions is better than for all data. In such conditions, R_e and K_C are greater than during fair weather conditions, and the values of C_D converge rapidly to a constant with limited spreading [30]. Moreover, C_D calculated over kelp (not extending over the full water column, unlike those presented in Table 3) range between 0.2 and 1 for K_C values ranging between 5 and 150 [39,74]. Such values are lower than that presented in Figure 7d.

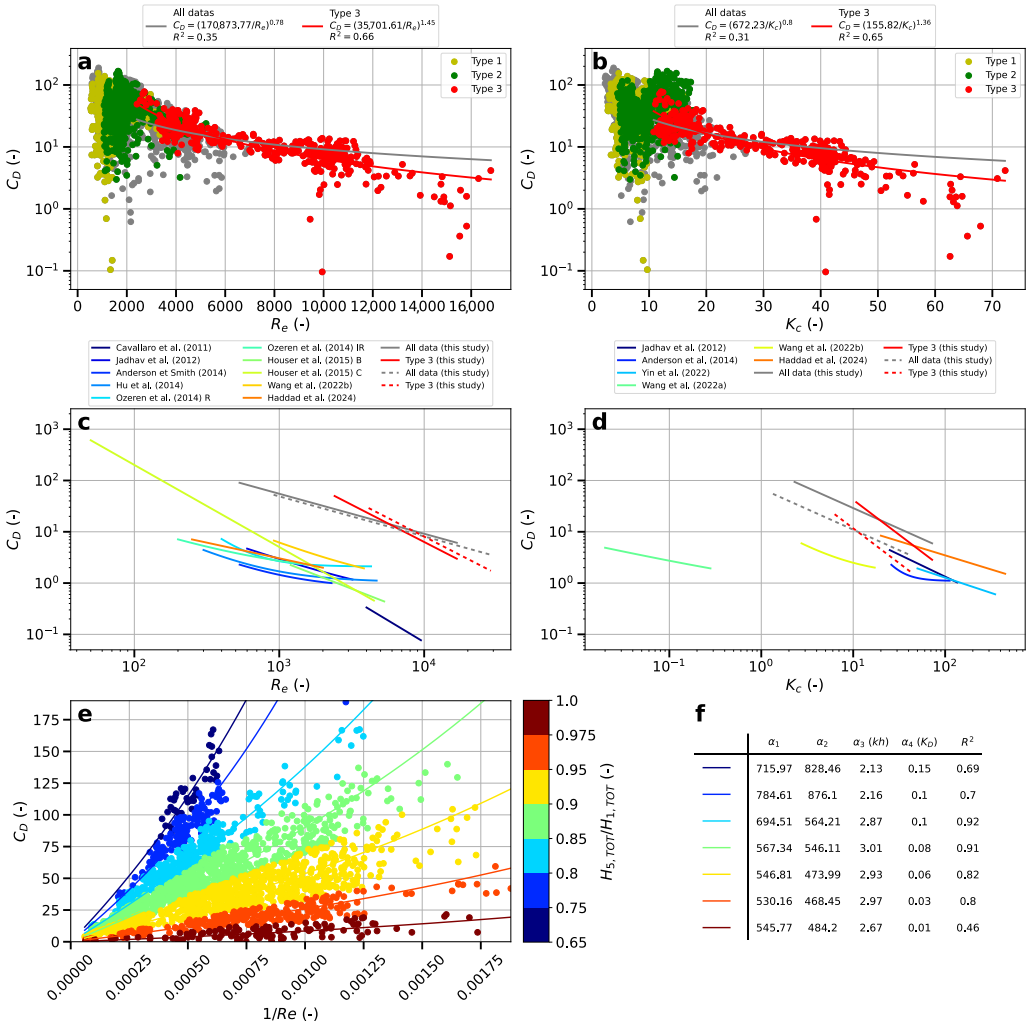

Figure 7. Empirical C_D represented as a function of the Reynolds R_e number (**a**) and the Keulegan–Carpenter K_C number (**b**) for all bursts. Bursts related to different meteo-marine condition types are represented by different colours. The grey dots represent bursts not related to the different meteo-marine condition types. Empirical C_D laws as a function of (**c**) R_e and (**d**) K_C in comparison with other analytical expression of C_D from the literature (see Table 3). Dashed lines represent the new empirical C_D laws calculated with the equivalent diameter volume D_V. Empirical C_D is shown as a function of $1/R_e$ (**e**). The colours represent the dissipation intervals over which the new fitted laws are calculated. The optimised parameters associated with each interval are presented in the table next to the plot (**f**).

In Figure 7c, the position of the experimental curves depends upon the features of the biomimetic structure, in particular, the diameter D. The relationships between C_D and R_e (or K_C) from the literature [30,34,40,56] are plotted for observed R_e in a range from 10^2 to 3×10^4, corresponding to aquatic vegetation with representative diameters in the order of a few centimetres. The C_D curves for the biomimetic structure (solid red and gray lines in Figure 7c,d) fit the extension in R_e of those extracted from the literature. They were derived for a representative diameter of $D = 3$ cm, not taking into account the fronds around the central main rope. However, the fronds occupy a significant volume in the water column and must contribute to the dissipation. Thus, the effect of fronds on C_D is overcome by redefining D.

Table 3. A list of relations between C_D and R_e or K_C presented in the literature. Type: L—laboratory study, I—in situ deployment, A—analytical/numerical modelling. u_c: characteristic velocity measured at the bottom (B) and top (T) of the structure. Wave: regular (R) or irregular (I) wave.

Reference	Type	Structure	Formulas	Ranges	u_c	Wave
Cavallaro et al. [56]	L	Artificial *Posidonia oceanica*	$C_D = (2100/R_e)^{1.7}$	$4000 < R_e < 9500$	T	R
Jadhav and Chen [30]	I	*Spartina alterniflora*	$C_D = 2(1300/R_e + 0.18)$	$600 < R_e < 3200$	B	I
			$C_D = 70{K_C}^{-0.86}$	$25 < K_C < 135$	B	I
Anderson and Smith [31]	L	Artificial *Spartina alterniflora*	$C_D = 0.76 + (744.2/R_e)^{1.27}$	$533 < R_e < 2296$	T	I
			$C_D = 1.1 + (27.4/K_C)^{3.08}$	$26 < K_C < 112$	T	I
Hu et al. [75]	L	Wooden rods	$C_D = 1.04 + (730/R_e)^{1.37}$	$300 < R_e < 4700$	T	R
Ozeren et al. [76]	L	Birch dowels	$C_D = 2.1 + (793/R_e)^{2.39}$	$400 < R_e < 4300$	T	R
			$C_D = 1.5 + (1230/R_e)^{0.95}$	$200 < R_e < 1600$	T	I
Houser et al. [22]	L	Semi-flexible balsa wood	$C_D = 0.001 + (2500/R_e)^{1.1}$	$1200 < R_e < 5300$	T	R
		Semi-flexible cable tie	$C_D = 0.001 + (2750/R_e)^{1.6}$	$50 < R_e < 4500$	T	R
Yin et al. [77]	A	Polyurethane cylinders	$C_D = (150.5/K_C)^{0.5952}$	$50 < K_C < 350$	T	R
Wang et al. [40]	L	PVC cylinder	$C_D = 0.42 + (0.77/K_C)^{0.41}$	$0.02 < K_C < 0.28$	T	R
Wang et al. [41]	L	PVC cylinder	$C_D = 0.75 + (4467.28/R_e)^{1.13}$	$918 < R_e < 3839$	T	R
			$C_D = 1.41 + (10.72/K_C)^{1.11}$	$2.74 < K_C < 17.14$	T	R
Haddad et al. [58]	I	*Spartina alterniflora*	$C_D = 207{R_e}^{-0.611}$	$250 < R_e < 2000$	T	I
			$C_D = 43.5{K_C}^{-0.549}$	$20 < K_C < 450$	T	I
Present study	I	Artificial kelp	$C_D = (170873.77/R_e)^{0.78}$	$532 < R_e < 16798$	T	I
			$C_D = (35701.61/R_e)^{1.45}$	$2410 < R_e < 16798$	T	I
			$C_D = (672.23/K_C)^{0.8}$	$2.3 < K_C < 72.2$	T	I
			$C_D = (155.82/K_C)^{1.36}$	$10.8 < K_C < 72.2$	T	I

A new diameter is defined as the volume-equivalent diameter D_V. Following Dalrymple et al. [52], D_V represents the diameter of a vertical rigid cylinder whose volume equals that of the solid portions constitutive of a biomimetic structure. D_V is calculated by digging a 1 m long portion of biomimetic structure in a known quantity of water and measuring the subsequent change in the water volume V. The expression of D_V is given by $D_V = \sqrt{4V/(\pi l_s)}$. Following this definition, the D_V calculated for a biomimetic structure is 5.15 cm. By applying the same approach as explained above, new empirical C_D laws are obtained (red and gray dashed–dotted lines in Figure 7c,d). Introducing D_V in the calculation of C_D results in a limited change in C_D as a function of R_e (Figure 7c) and a more significant effect on C_D as a function of K_C (Figure 7d), and does not improve the correlation coefficients. Last, C_D calculated with or without D_V is in the range of the values found in the literature.

Alternatively, we investigate how to improve the correlation coefficient R^2 of the empirical C_D laws (Figure 7a,b) by bypassing the existing uncertainties on parameters S_{ref}, D, l_s, K_D and h. In doing so, we highlight the parameters that clearly control variations in C_D together with R_e (resp. K_C) as C_D values vary widely. Figure 7e shows C_D as a function of $1/R_e$ for different ranges of the total dissipation measured through the biomimetic solution. For a given $1/R_e$, C_D increases with the total dissipation $H_{5,TOT}/H_{1,TOT}$, and thus, with K_D through Equations (4) and (5). From this observation, a new expression for C_D is proposed. Equation (5) is rewritten to express C_D as a function of K_D. The term $\sinh kh$ appears and is rewritten as a function of the Reynolds number R_e and orbital velocity thanks to Equation (7), so that

$$C_D = \alpha_4 \alpha_1 \left(\frac{\alpha_2 \alpha_3}{R_e} + \left(\frac{\alpha_2}{R_e} \right)^2 \sqrt{\left(\frac{\alpha_2}{R_e} \right)^2 + 1} \right) \tag{11}$$

where $\alpha_1 = \frac{9\pi}{2kS_{ref}(\sinh kl_s{}^3 + 3\sinh kl_s)}$, $\alpha_2 = \frac{\pi H_{s0} D}{Tv} \cosh kl_s$, $\alpha_3 = kh$ and $\alpha_4 = K_D$.

The experimental bursts are classified in seven intervals of $H_{5,TOT}/H_{1,TOT}$ values. It appears that these intervals follow a clear organisation (Figure 7e), which introduces some control of C_D by the parameters, leading to dissipation. For each dissipation interval, a C_D law is calculated following Equation (11). Parameters α_1 to α_4 are set by numerical optimization, specifically using a nonlinear least squares method, using the Python module scipy.optimise. Figure 7f shows the optimal parameters and the associated correlation coefficients for the seven C_D laws. First, except for extremely low dissipation rates, the coefficient correlation R^2 obtained from Equation (11) is clearly better than that from the initial formulation. This can be explained by the fact that the formalism of Kobayashi et al. [34] relies mostly on data from flume experimentation, where dissipation is explored in a restrictive range and fails to capture the spreading of C_D. When field data are available, Equation (11) can be advantageously used to provide a more suitable value of C_D.

Defining an experimental C_D as a function of wave dissipation, while analytical laws of wave dissipation all rely on the expression of C_D , is somewhat paradoxical. However, this paradox can be easily resolved keeping in mind that determining experimental C_D and using the analytical C_D law do not serve the same purpose. Analytical C_D laws are essentially used in numerical modelling to reproduce the bottom friction effect, whereas experimental C_D is used to characterise the protection solution's resistance against the fluid, in other words, the dissipation properties of the solution. For a given solution, experimental C_D obtained under various forcing conditions can be resumed by an experimental law. The law proposed in Equation (11) enables C_D to be adjusted for the solution studied, whose geometric parameters are already known, as is the hydrodynamic context in which it is set. In such a context, coastal managers who would plan to deploy the studied solution have the opportunity to estimate C_D, without carrying out any experimentation. More generally, the design of an innovative protection solution would be improved by performing a systematic field campaign on wave dissipation over the solution, providing an adapted C_D law for this solution.

6. Conclusions and Perspectives

In this paper, a set of pressure time series is used to explore frequency-dependent wave energy dissipation over a biomimetic, soft, artificial solution that emulates natural kelps. The dissipation is calculated from the theory of Dalrymple et al. [52] on a flat bottom under the assumption that the structure studied, made of central vertical rope extending from the bottom to surface of the water, to which two fronds are tied at regular 10 cm intervals, although complex and fully flexible, can be represented by a rigid cylinder.

The wave height decays by 10%, whatever the meteo-marine forcing recorded. Such a reduction is attributed to the presence of the biomimetic solution, since it is located far from the breaking zone and bottom friction is negligible. However, these parameters were

estimated and could not be measured directly in the field. A preliminary deployment without the protection solution would allow the bottom friction to be quantified. As the deployment zone is located in a sensitive site where authorisations must be obtained to install an instrumental device, no preliminary deployment could be carried out.

Wave dissipation shows frequency dependence. Infragravity waves gain up to 35% of their energy through the biomimetic solution, unlike swell and shorter waves that are attenuated by up to 25%. Energy variations in each frequency band must be explained by the action of the biomimetic structure and not by frequency band-to-band energy transfer, shoaling or bottom friction. Moreover, stationary waves are trapped within the biomimetic solution and have an anti-dissipative effect at the lee side of the solution for forcing conditions with frequencies close to the first resonant mode. Last, the biomimetic solution cannot be seen as a wall of a semi-enclosed basin extending from the solution toward the beach or toward the dyke. In addition, no pressure sensors were deployed beyond the biomimetic solution. No measurements were taken to determine if resonant waves propagate outside the biomimetic solution, which could have helped verify whether the solution can be considered as a wall.

To handle the complex geometry of a biomimetic structure in the expression of the drag coefficient C_D, the concept of volume-equivalent diameter D_V is defined as the diameter of a vertical rigid cylinder whose volume is equal to the volume of the solid portion of the biomimetic structure. However, introducing D_V does not significantly change the values of C_D with respect to R_e or K_C and does not improve the correlation. Alternatively, a last type of C_D law is explored, which relies on four parameters (combinations of wave and geometrical properties). For several subsets of C_D values for distinct ranges of dissipation ratio, the four parameters are calculated by optimization and define C_D laws with correlation coefficients slightly improved with respect to the expression of [34]. These new C_D laws, depending upon the dissipative properties of the biomimetic solution, could be advantageous when the characterization of a biomimetic solution's dissipative properties relies on field observation, or improve the C_D interval in the design of such a solution. However, further studies under in situ conditions are needed to test this new empirical law, as well as to share the measurements made on wave dissipation and frequency dependence through flexible protection solutions.

In the future, the design of biomimetic solution geometry must deal with the increase in both IG and trapped waves. These processes may be explored further with a numerical model to test different conditions, such as the placement and density of the modules, with the aim of (i) limiting the increase in long-wave energy and (ii) maximising wave dissipation.

Author Contributions: Conceptualization, methodology, software, validation, formal analysis, investigation, writing—original draft, writing—review and editing and visualization were contributed to by G.M. Conceptualization, validation, resources, writing—review and editing and funding acquisition were contributed to by F.B. Conceptualization, validation, investigation and writing—review and editing were contributed to by S.M. Writing—review and editing was contributed to by R.C. Resources and funding acquisition were contributed to by J.-Y.J. All authors have read and agreed to the published version of the manuscript.

Funding: This work was conducted as part of the PhD of Ms. Marlier, funded by P2A Développement and ANRT (CIFRE grant number 2021/1086). The project has been funded by the Occitanie Region, Plan Littoral 2021 and Caisse des Dépôts.

Institutional Review Board Statement: Not applicable.

Informed Consent Statement: Not applicable.

Data Availability Statement: The data used in this article are available upon reasonable request to the corresponding author, until they are deposited in a permanent repository.

Acknowledgments: We would like to thank P2A Développement, who allowed us to study their biomimetic structures. We would also like to thank the research group GLADYS (www.gladys-littoral.org) for the equipment provided during the field campaign.

Conflicts of Interest: G. Marlier was employed by P2A Développement. The remaining authors declare that the research was conducted in the absence of any commercial or financial relationships that could be construed as a potential conflict of interest.

Abbreviations

The following abbreviations are used in this manuscript:

SSE	Soft-shoreline engineering
IG	Infragravity frequency band
SS	Swell frequency band
WW	Wind wave frequency band
TOT	Total frequency band on wave spectrum

References

1. Bruun, P. The history and philosophy of coastal protection. In *Coastal Engineering 1972*; American Society of Civil Engineers: Reston, VA, USA, 1972; pp. 33–74. [CrossRef]
2. Caulk, A.D.; Gannon, J.E.; Shaw, J.R.; Hartig, J.H. Best Management Practices for Soft Engineering of Shorelines. Greater Detroit American Heritage River Initiative. 2000. Available online: https://www.semcog.org/desktopmodules/SEMCOG.Publications/GetFile.ashx?filename=BestManagementPracticesForSoftEngineeringOfShorelinesSeptember2000.pdf (accessed on 13 October 2024).
3. Hartig, J.; Zarull, M.; Cook, A. Soft shoreline engineering survey of ecological effectiveness. *Ecol. Eng.* **2011**, *37*, 1231–1238. [CrossRef]
4. Douglass, S.L.; Pickel, B.H. The Tide Doesn't Go Out Anymore- The Effect of Bulkheads on Urban Bay Shorelines. *Shore Beach* **1999**, *67*, 19–25.
5. Govarets, A.; Lauwerts, B. Assessment of the Impact of Coastal Defence Structures. Biodiversity Series: OSPAR Commission. 2009. Available online: https://qsr2010.ospar.org/media/assessments/p00435_Coastal_defence.pdf (accessed on 13 October 2024).
6. Sutton-Grier, A.E.; Wowk, K.; Bamford, H. Future of our coasts: The potential for natural and hybrid infrastructure to enhance the resilience of our coastal communities, economies and ecosystems. *Environ. Sci. Policy* **2015**, *51*, 137–148. [CrossRef]
7. Morris, R.L.; Konlechner, T.M.; Ghisalberti, M.; Swearer, S.E. From grey to green: Efficacy of eco-engineering solutions for nature-based coastal defence. *Glob. Chang. Biol.* **2018**, *24*, 1827–1842. [CrossRef]
8. Silva, R.; Mendoza, E.; Mariño-Tapia, I.; Martínez, M.L.; Escalante, E. An artificial reef improves coastal protection and provides a base for coral recovery. *J. Coast. Res.* **2016**, *75*, 467–471. [CrossRef]
9. Perricone, V.; Mutalipassi, M.; Mele, A.; Buono, M.; Vicinanza, D.; Contestabile, P. Nature-based and bioinspired solutions for coastal protection: An overview among key ecosystems and a promising pathway for new functional and sustainable designs. *ICES J. Mar. Sci.* **2023**, *80*, fsad080. [CrossRef]
10. Narayan, S.; Beck, M.W.; Reguero, B.G.; Losada, I.J.; Van Wesenbeeck, B.; Pontee, N.; Sanchirico, J.N.; Ingram, J.C.; Lange, G.M.; Burks-Copes, K.A. The effectiveness, costs and coastal protection benefits of natural and nature-based defences. *PLoS ONE* **2016**, *11*, e0154735. [CrossRef]
11. Mullarney, J.C.; Henderson, S.M. Flows within marine vegetation canopies. In *Advances in Coastal Hydraulics*; World Scientific Publishing Ltd.: Singapore, 2018; pp. 1–46.
12. Katiyar, N.K.; Goel, G.; Hawi, S.; Goel, S. Nature-inspired materials: Emerging trends and prospects. *NPG Asia Mater.* **2021**, *13*, 56. [CrossRef]
13. Nowacki, D.J.; Beudin, A.; Ganju, N.K. Spectral wave dissipation by submerged aquatic vegetation in a back-barrier estuary: Wave dissipation by vegetation. *Limnol. Oceanogr.* **2017**, *62*, 736–753. [CrossRef]
14. Tuya, F.; Vila, F.; Bergasa, O.; Zarranz, M.; Espino, F.; Robaina, R.R. Artificial seagrass leaves shield transplanted seagrass seedlings and increase their survivorship. *Aquat. Bot.* **2017**, *136*, 31–34. [CrossRef]
15. Ghisalberti, M.; Nepf, H.M. Mixing layers and coherent structures in vegetated aquatic flows. *J. Geophys. Res. Oceans* **2002**, *107*, 3-1–3-11. [CrossRef]
16. Luhar, M.; Coutu, S.; Infantes, E.; Fox, S.; Nepf, H. Wave-induced velocities inside a model seagrass bed. *J. Geophys. Res. Oceans* **2010**, *115*, C12005. [CrossRef]
17. Tang, C.; Yi, Y.; Zhang, S. Flow and turbulence in unevenly obstructed channels with rigid and flexible vegetation. *J. Environ. Manag.* **2023**, *326*, 116736. [CrossRef] [PubMed]
18. Pujol, D.; Nepf, H. Breaker-generated turbulence in and above a seagrass meadow. *Cont. Shelf Res.* **2012**, *49*, 1–9. [CrossRef]

19. Tinoco, R.O.; Coco, G. Turbulence as the Main Driver of Resuspension in Oscillatory Flow Through Vegetation. *J. Geophys. Res. Earth Surf.* **2018**, *123*, 891–904. [CrossRef]
20. Wu, C.; Wu, S.; Wu, X.; Zhang, Y.; Feng, K.; Zhang, W.; Zhao, Y. Hydrodynamics affected by submerged vegetation with different flexibility under unidirectional flow. *Front. Mar. Sci.* **2023**, *9*, 1041351. [CrossRef]
21. Mendez, F.J.; Losada, I.J. An empirical model to estimate the propagation of random breaking and nonbreaking waves over vegetation fields. *Coast. Eng.* **2004**, *51*, 103–118. [CrossRef]
22. Houser, C.; Trimble, S.; Morales, B. Influence of Blade Flexibility on the Drag Coefficient of Aquatic Vegetation. *Estuaries Coasts* **2015**, *38*, 569–577. [CrossRef]
23. van Veelen, T.J.; Fairchild, T.P.; Reeve, D.E.; Karunarathna, H. Experimental study on vegetation flexibility as control parameter for wave damping and velocity structure. *Coast. Eng.* **2020**, *157*, 103648. [CrossRef]
24. Chen, S.N.; Sanford, L.P.; Koch, E.W.; Shi, F.; North, E.W. A nearshore model to investigate the effects of seagrass bed geometry on wave attenuation and suspended sediment transport. *Estuaries Coasts* **2007**, *30*, 296–310. [CrossRef]
25. Hansen, J.C.; Reidenbach, M.A. Wave and tidally driven flows in eelgrass beds and their effect on sediment suspension. *Mar. Ecol. Prog. Ser.* **2012**, *448*, 271–287. [CrossRef]
26. Ganthy, F.; Soissons, L.; Sauriau, P.G.; Verney, R.; Sottolichio, A. Effects of short flexible seagrass Zostera noltei on flow, erosion and deposition processes determined using flume experiments. *Sedimentology* **2015**, *62*, 997–1023. [CrossRef]
27. Liu, C.; Shan, Y.; Nepf, H. Impact of Stem Size on Turbulence and Sediment Resuspension Under Unidirectional Flow. *Water Resour. Res.* **2021**, *57*, e2020WR028620. [CrossRef]
28. Reguero, B.G.; Beck, M.W.; Agostini, V.N.; Kramer, P.; Hancock, B. Coral reefs for coastal protection: A new methodological approach and engineering case study in Grenada. *J. Environ. Manag.* **2018**, *210*, 146–161. [CrossRef]
29. Ghiasian, M.; Carrick, J.; Rhode-Barbarigos, L.; Haus, B.; Baker, A.C.; Lirman, D. Dissipation of wave energy by a hybrid artificial reef in a wave simulator: Implications for coastal resilience and shoreline protection. *Limnol. Oceanogr. Methods* **2021**, *19*, 1–7. [CrossRef]
30. Jadhav, R.S.; Chen, Q. Field investigation of wave dissipation over salt marsh vegetation during tropical cyclone. *Int. Conf. Coastal. Eng.* **2012**, *1*, 41. [CrossRef]
31. Anderson, M.; Smith, J. Wave attenuation by flexible, idealized salt marsh vegetation. *Coast. Eng.* **2014**, *83*, 82–92. [CrossRef]
32. Zhang, X.; Lin, P.; Nepf, H. A simple-wave damping model for flexible marsh plants. *Limnol. Oceanogr.* **2021**, *66*, 4182–4196. [CrossRef]
33. Zhang, X.; Nepf, H. Reconfiguration of and drag on marsh plants in combined waves and current. *J. Fluids Struct.* **2022**, *110*, 103539. [CrossRef]
34. Kobayashi, N.; Raichle, A.W.; Asano, T. Wave Attenuation by Vegetation. *J. Waterway Port Coastal Ocean Eng.* **1993**, *119*, 30–48. [CrossRef]
35. Dubi, A.; Tørum, A. Wave damping by kelp vegetation. In *Coastal Engineering 1994*; American Society of Civil Engineers: Reston, VA, USA, 1995; pp. 142–156. [CrossRef]
36. Bradley, K.; Houser, C. Relative velocity of seagrass blades: Implications for wave attenuation in low-energy environments. *J. Geophys. Res.* **2009**, *114*, F01004. [CrossRef]
37. Paul, M.; Amos, C.L. Spatial and seasonal variation in wave attenuation over *Zostera noltii*. *J. Geophys. Res.* **2011**, *116*, C08019. [CrossRef]
38. Lei, J.; Nepf, H. Wave damping by flexible vegetation: Connecting individual blade dynamics to the meadow scale. *Coast. Eng.* **2019**, *147*, 138–148. [CrossRef]
39. Zhu, L.; Huguenard, K.; Fredriksson, D.W.; Lei, J. Wave attenuation by flexible vegetation (and suspended kelp) with blade motion: Analytical solutions. *Adv. Water Resour.* **2022**, *162*, 104148. [CrossRef]
40. Wang, Y.; Yin, Z.; Liu, Y. Experimental investigation of wave attenuation and bulk drag coefficient in mangrove forest with complex root morphology. *Appl. Ocean Res.* **2022**, *118*, 102974. [CrossRef]
41. Wang, Y.; Yin, Z.; Liu, Y. Laboratory study on the drag coefficient for mangrove forests in regular waves. *Ocean Eng.* **2022**, *255*, 111522. [CrossRef]
42. van Veelen, T.J.; Karunarathna, H.; Reeve, D.E. Modelling wave attenuation by quasi-flexible coastal vegetation. *Coast. Eng.* **2021**, *164*, 103820. [CrossRef]
43. Yin, K.; Xu, S.; Huang, W.; Liu, S.; Li, M. Numerical investigation of wave attenuation by coupled flexible vegetation dynamic model and XBeach wave model. *Ocean Eng.* **2021**, *235*, 109357. [CrossRef]
44. Beth Schaefer, R.; Nepf, H. Wave damping by seagrass meadows in combined wave-current conditions. *Limnol. Oceanogr.* **2022**, *67*, 1554–1565. [CrossRef]
45. Méndez, F.J.; Losada, I.J.; Losada, M.A. Hydrodynamics induced by wind waves in a vegetation field. *J. Geophys. Res.* **1999**, *104*, 18383–18396. [CrossRef]
46. Maza, M.; Lara, J.L.; Losada, I.J. A coupled model of submerged vegetation under oscillatory flow using Navier–Stokes equations. *Coast. Eng.* **2013**, *80*, 16–34. [CrossRef]
47. Henderson, S.M. Motion of buoyant, flexible aquatic vegetation under waves: Simple theoretical models and parameterization of wave dissipation. *Coast. Eng.* **2019**, *152*, 103497. [CrossRef]

48. Lindhart, M.; Daly, M.; Walker, H.; Arzeno-Soltero, I.B.; Yin, J.; Bell, T.W.; Monismith, S.G.; Pawlak, G.; Leichter, J. Short wave attenuation by a kelp forest canopy. *Limnol. Oceanogr. Lett.* **2024**, *9*, 478–486. [CrossRef]
49. Elwany, M.H.S.; O'Reilly, W.C.; Guza, R.T.; Flick, R.E. Effects of Southern California Kelp Beds on Waves. *J. Waterway Port Coastal Ocean Eng.* **1995**, *121*, 143–150. [CrossRef]
50. Rosman, J.H.; Koseff, J.R.; Monismith, S.G.; Grover, J. A field investigation into the effects of a kelp forest (Macrocystis pyrifera) on coastal hydrodynamics and transport. *J. Geophys. Res. Oceans* **2007**, *112*, C02016. [CrossRef]
51. Elsmore, K.; Nickols, K.J.; Miller, L.P.; Ford, T.; Denny, M.W.; Gaylord, B. Wave damping by giant kelp, Macrocystis pyrifera. *Ann. Bot.* **2024**, *133*, 29–40. [CrossRef]
52. Dalrymple, R.A.; Kirby, J.T.; Hwang, P.A. Wave Diffraction Due to Areas of Energy Dissipation. *J. Waterway Port Coastal Ocean Eng.* **1984**, *110*, 67–79. [CrossRef]
53. Morison, J.; Johnson, J.W.; Schaaf, S.A. The force exerted by surface waves on piles. *J. Pet. Technol.* **1950**, *2*, 149–154. [CrossRef]
54. Luhar, M.; Infantes, E.; Nepf, H. Seagrass blade motion under waves and its impact on wave decay. *J. Geophys. Res. Oceans* **2017**, *122*, 3736–3752. [CrossRef]
55. Keulegan, G.; Carpenter, L. Forces on cylinders and plates in an oscillating fluid. *J. Res. Natl. Bur. Stand.* **1958**, *60*, 423. [CrossRef]
56. Cavallaro, L.; Re, C.L.; Paratore, G.; Viviano, A.; Foti, E. Response of posidonia oceanica to wave motion in shallow-waters-preliminary experimental results. *Coast. Eng. Proc.* **2011**, *1*, 49. [CrossRef]
57. Cavallaro, L.; Viviano, A.; Paratore, G.; Foti, E. Experiments on Surface Waves Interacting with Flexible Aquatic Vegetation. *Ocean Sci. J.* **2018**, *53*, 461–474. [CrossRef]
58. Haddad, J.; Rosman, J.H.; Luettich, R.A.; Voss, C.M. Canopy drag parameterization from field observations for modeling wave transformation across salt marshes. *Coast. Eng.* **2024**, *187*, 104407. [CrossRef]
59. Luhar, M.; Nepf, H. Wave-induced dynamics of flexible blades. *J. Fluids Struct.* **2016**, *61*, 20–41. [CrossRef]
60. Luhar, M.; Nepf, H.M. Flow-induced reconfiguration of buoyant and flexible aquatic vegetation. *Limnol. Oceanogr.* **2011**, *56*, 2003–2017. [CrossRef]
61. Suzuki, T.; Zijlema, M.; Burger, B.; Meijer, M.C.; Narayan, S. Wave dissipation by vegetation with layer schematization in SWAN. *Coast. Eng.* **2012**, *59*, 64–71. [CrossRef]
62. Jacobsen, N.; McFall, B.; van der A, D. A frequency distributed dissipation model for canopies. *Coast. Eng.* **2019**, *150*, 135–146. [CrossRef]
63. Ascencio, J.A.; Jacobsen, N.G.; McFall, B.C.; Groeneweg, J.; Vuik, V.; Reniers, A.J. Evaluation of Implicit and Explicit Wave Dissipation Models for Submerged and Emergent Aquatic Vegetation. *J. Coast. Res.* **2022**, *38*, 807–815. [CrossRef]
64. Horikawa, K. Nearshore Dynamics and Coastal Processes: Theory. In *Measurement, and Predictive Models*; University of Tokyo Press: Tokyo, Japan, 1988.
65. Bertin, X.; de Bakker, A.; Van Dongeren, A.; Coco, G.; André, G.; Ardhuin, F.; Bonneton, P.; Bouchette, F.; Castelle, B.; Crawford, W.C.; et al. Infragravity waves: From driving mechanisms to impacts. *Earth-Sci. Rev.* **2018**, *177*, 774–799. [CrossRef]
66. Massel, S.R. *Ocean Surface Waves: Their Physics and Prediction*; World Scientific: Singapore, 1996; Volume 11.
67. Munk, W.H. The solitary wave theory and its application to surf problems. *Ann. N. Y. Acad. Sci.* **1949**, *51*, 376–424. [CrossRef]
68. Nelson, R. Height limits in top down and bottom up wave environments. *Coast. Eng.* **1997**, *32*, 247–254. [CrossRef]
69. Guo, J. Simple and explicit solution of wave dispersion equation. *Coast. Eng.* **2002**, *45*, 71–74. [CrossRef]
70. Hedges, T. Regions of validity of analytical wave theories. *Oceanogr. Lit. Rev.* **1996**, *1*, 10. [CrossRef]
71. Mayençon, R. *Météorologie Marine*, 2nd ed.; Éditions Maritimes et d'Outre-Mer: Paris, France, 1992.
72. Phillips, O. The Dynamics of the Upper Ocean. In *Cambridge Monographs on Mechanics and Applied Mathematics*; Cambridge University Press: Cambridge, UK, 1966; pp. 244–255.
73. Rabinovich, A.B. Seiches and Harbor Oscillations. In *Handbook of Coastal and Ocean Engineering*; World Scientific: Singapore, 2010. [CrossRef]
74. Zhu, L.; Lei, J.; Huguenard, K.; Fredriksson, D.W. Wave attenuation by suspended canopies with cultivated kelp (*Saccharina latissima*). *Coast. Eng.* **2021**, *168*, 103947. [CrossRef]
75. Hu, Z.; Suzuki, T.; Zitman, T.; Uittewaal, W.; Stive, M. Laboratory study on wave dissipation by vegetation in combined current–wave flow. *Coast. Eng.* **2014**, *88*, 131–142. [CrossRef]
76. Ozeren, Y.; Wren, D.G.; Wu, W. Experimental Investigation of Wave Attenuation through Model and Live Vegetation. *J. Waterway Port Coast. Ocean Eng.* **2014**, *140*, 04014019. [CrossRef]
77. Yin, K.; Xu, S.; Gong, S.; Chen, J.; Wang, Y.; Li, M. Modeling wave attenuation by submerged flexible vegetation with XBeach phase-averaged model. *Ocean Eng.* **2022**, *257*, 111646. [CrossRef]